Materials and Design 186 (2020) 108372

Contents lists available at ScienceDirect

Materials and Design

journal homepage: www.elsevier.com/locate/matdes

Advanced heat treated die-cast aluminium composites fabricated by TiB_2 nanoparticle implantation

Xixi Dong [a], Hamza Youssef [a], Yijie Zhang [a], Hailin Yang [b], Shihao Wang [a], Shouxun Ji [a,*]

[a] *Brunel Centre for Advanced Solidification Technology (BCAST), Institute of Materials and Manufacturing, Brunel University London, Uxbridge UB8 3PH, United Kingdom*
[b] *State Key Laboratory of Powder Metallurgy, Central South University, Changsha 410083, China*

HIGHLIGHTS

- Super vacuum of 20 mbar was achieved in limited evacuation time of 1.6 s during die casting of AlSiMgMn/TiB_2 composites.
- Heat-treated AlSiMgMn/3.5wt.%TiB_2 composite had yield strength of 351MPa, tensile strength of 410MPa and ductility of 5.2%.
- Die castability of compsites decreased with increasing of TiB_2 nanoparticles due to decrease of die filling ability.
- Strengthening of heat-treated AlSiMgMn/TiB_2 composites resulted from TiB_2 nanoparticles and β″ precipitates.

GRAPHICAL ABSTRACT

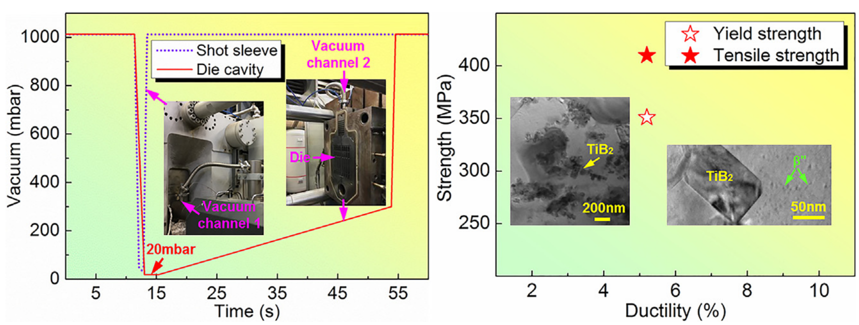

ARTICLE INFO

Article history:
Received 2 August 2019
Received in revised form 13 November 2019
Accepted 15 November 2019
Available online xxxx

Keywords:
Aluminium alloy
High pressure die casting
Super vacuum
Nano reinforcement

ABSTRACT

The global carbon emission reduction strongly requires high strength lightweight die-cast aluminium alloys in industry. Here die-cast AlSiMgMn–TiB_2 composites with advanced mechanical performance were fabricated by the implantation of TiB_2 nanoparticles. Super vacuum assisted high pressure die casting was applied to enable the T6 heat treatment of the composites, and the super vacuum of 20 mbar was achieved in the limited evacuation time of 1.6 s. The composites demonstrated good die castability within the addition of 3.5 wt% TiB_2, while the composites could not fill into the chill vent with the addition of >3.5 wt% TiB_2. The composite with 3.5 wt% TiB_2 nanoparticles delivered the high hardness of 150.2 kg/mm^2, yield strength of 351 MPa, tensile strength of 410 MPa, and the industrially applicable good ductility of 5.2%, after T6 heat treatment. The strengthening of the T6 heat treated composite was a result of both TiB_2 nanoparticles and nanoscale β″ precipitates that had coherent interfaces with α–Al matrix, i.e., Al(11-1)//TiB_2(0001), Al[011]//TiB_2[11-20], Al[320]//β″(*a*-axis), Al[1-30]//β″(*c*-axis) and Al(020)//β″(*b*-axis). The T6 heat treated composite reinforced by 3.5 wt% TiB_2 showed ductile fracture.

1. Introduction

High pressure die casting (HPDC) is a near-net shape manufacturing process in which the molten die-cast metal is injected into a metal die cavity at high speed and solidified under high pressure [1,2]. HPDC has been widely used in producing lightweight die-cast aluminium and magnesium alloy components with high dimensional accuracy, high production efficiency and low-cost for automotive and other industries [3–6]. The turbulent flow under high speed injection and the consequent entrapment of air during die filling are inherent problems for the currently used conventional non-vacuum assisted HPDC process,

* Corresponding author.
E-mail address: shouxun.ji@brunel.ac.uk (S. Ji).

https://doi.org/10.1016/j.matdes.2019.108372

which lead to the formation of gas porosities in HPDC castings [7]. The gas porosities will expand and blister when exposed to high temperatures, which makes the conventional HPDC castings unavailable for further strengthening through high temperature heat treatment. Therefore the majority of the HPDC castings have to be used in as-cast state. In recent years, the world-wide consensus of the reducing of carbon emission strongly motivates the lightweight of automobile, which requires the die-cast aluminium alloys to be able to provide higher strength, for the achieving of the structural weight saving through the use of the thinner wall components basing on stronger alloys [8]. However, the as-cast strengths of the currently available die-cast automotive aluminium alloys are usually low, with a yield strength of ~130–170 MPa [9,10]. Explorations have been done to develop die-cast automotive aluminium alloys with higher strength by conventional micro alloying, but the improvements are struggling limited and the improved yield strengths are still in the low level of 180–190 MPa [11–14]. It is hard to meet the requirement of higher strength die-cast automotive aluminium alloys basing on the currently available alloys.

The particle reinforcement has been proved effective for the strengthening of materials [15–18]. For cast aluminium alloys, ceramic particles such as TiB_2, Al_2O_3, Si_3N_4, TiC, SiC and AlN have been added to strengthen the alloys [19–24]. However, few literatures reported the particle reinforcement of the die-cast aluminium alloys under HPDC [25]. Among the available ceramic reinforcement particles for casting, TiB_2 has high Young's modulus and wets with molten aluminium, and TiB_2 can be in-situ synthesized in the molten aluminium with a size of nanoscale [26]. So TiB_2 nanoparticles were chosen here to reinforce the die-cast aluminium alloys. Furthermore, the latest developed frontier super vacuum assisted HPDC process can achieve a cutting-edge vacuum [27], and it could largely decrease the gas porosities in HPDC castings and enable the further strengthening of the die-cast aluminium alloys through heat treatment.

Al–Si–Mg–Mn die-cast aluminium alloys have been widely used in automotive industry for the manufacturing of high integrity castings due to excellent combinations of castability, strength, ductility and corrosion resistance [9,11,28]. The focus of this study is the introduction of TiB_2 nanoparticle on the reinforcement of the die-cast AlSiMgMn alloy, for the achieving of advanced heat-treated die-cast AlSiMgMn–TiB_2 composites. Super vacuum assisted HPDC was applied to enable the heat treatment of the composites.

2. Experimental

2.1. Melts preparation

The designed die-cast AlSiMgMn–TiB_2 composites, with the actual compositions (in wt%) of Al9Si0.6Mg0.6Mn0.18Fe0.12Ti–xTiB_2 ($x = 0$, 1.5, 3.5), were melted in a clay-graphite crucible using the electric resistance furnace. The ingot of pure Al was first melted, then the ingot of pure Mg and the master alloys of Al–50 wt% Si, Al–20 wt% Mn, Al–45 wt % Fe and Al–10 wt% Ti were added into the molten Al to achieve the designed composition. After the TiB_2 ceramic nanoparticles with the desired amounts were added into the melts through the addition of the Al–10 wt% TiB_2 master alloy. The details of the TiB_2 nanoparticles in the Al–10 wt% TiB_2 master alloy are presented in Section 3.1. During melting, the temperature of the furnace was controlled at 750 °C. After melting, the Al–10 wt% Sr master alloy was added into the melts to achieve the Sr content of 200 ppm, for the modification of the morphology of the eutectic Si phase during solidification. Then the melts were degassed through injecting pure argon into the melts by using a rotary degassing impeller at a speed of 350 rpm for 5 min, and the melts were ready for HPDC afterwards.

2.2. Frontier super vacuum assisted HPDC

Fig. 1 shows the latest developed frontier two-stage super vacuum assisted HPDC process used for the fabrication of the die-cast AlSiMgMn–TiB_2 composites. Different from the conventional one-stage vacuum by evacuation only from the die cavity, here the two-stage vacuum was applied by evacuation from both the shot sleeve and the die cavity simultaneously, and eight ASTM B557 standard round tensile test bars with a gauge dimension of ϕ6.35 mm × 50 mm were casted in the die cavity under each HPDC shot, as shown in Fig. 1a. Fig. 1b presents the vacuum curves showing the evolutions of the vacuum in the shot sleeve and the die cavity during a complete HPDC cycle, and the cutting-edge super vacuum of 20 mbar was achieved in the die cavity in limited evacuation time of 1.6 s, which was far below the commonly achieved vacuum of ~50–100 mbar by the conventional one-stage evacuation process [29–31]. The details of this frontier two-stage super vacuum assisted HPDC were introduced in our latest report [27]. The HPDC experiments were conducted on a 4500 kN cold chamber HPDC machine. The HPDC die was heated by the circulation of the 250 °C mineral oil, and the die temperature was ~230 °C. The prepared alloy melts were loaded into the shot sleeve for HPDC. The pouring temperature of melts was controlled at 690 °C by thermocouple, and the holding pressure was controlled at 320 bar.

2.3. Heat treatment and mechanical tests

The as-cast tensile test bars were subjected to T6 heat treatment, which included solid solution and the subsequent peak artificial ageing [32]. Differential scanning calorimetry (DSC) analysis was conducted on a TA instrument Q800 with a heating rate of 10 °C/min, to determine the solution temperature. Solution treatment was carried out at 540 °C for 30 min, followed by immediate water quenching. Ageing treatment was conducted at 170 °C. Vickers hardness tests were performed on a FM-800 tester with an applied load of 10 kg for 10 s, to determine the peak ageing time. The T6 heat-treated bars were pulled on an Instron 5500 machine at room temperature. The extensometer was applied for the monitoring of the strain during tensile tests. The ramp rate for extension was set as 1 mm/min. Each tensile data reported with standard deviation was based on the testing of at least twelve samples.

2.4. Microstructure characterization

The microstructure was examined using the Zeiss SUPRA 35VP scanning electron microscope (SEM) equipped with electron backscatter diffraction (EBSD), and the JEOL-2100 transmission electron microscopy (TEM). The microstructure characterization of the samples was taken from the gauge length section of the tensile test bars. The samples for SEM morphology analysis were prepared following the standard grinding and polishing process, and then etching with the standard Keller's solution. The samples for EBSD analysis were prepared by vibration polishing at a frequency of 90 Hz for three hours after the standard grinding and polishing. Thin specimens for TEM observation were prepared by ion beam polishing on a Gatan Precision Ion Polishing System (PIPS, Gatan model 691). A constant preparation temperature of −10 °C was maintained during the ion beam polishing. TEM operating at 200 kV was used for bright-field imaging, select area diffraction pattern (SADP) analysis and high-resolution transmission electron microscopy (HRTEM) imaging.

3. Results & discussion

3.1. Al–TiB_2 master alloy with TiB_2 nanoparticles

The Al–10wt.%TiB_2 master alloy was self-synthesized through the in-situ reaction [33] between the K_2TiF_6 and KBF_4 salts in the molten Al at ~850 °C. The TiB_2 ceramic nanoparticles were formed during the reaction, and remained in the Al–10wt.%TiB_2 master alloy after solidification. Fig. 2a presents the SEM morphology of the Al–10wt.%TiB_2 master alloy, and TiB_2 nanoparticles dispersed homogeneously in the Al matrix of the master alloy. Fig. 2b shows the bright-field TEM morphology of the TiB_2 nanoparticle in the Al–10wt.%TiB_2 master alloy. Fig. 2c presents the SADP of the

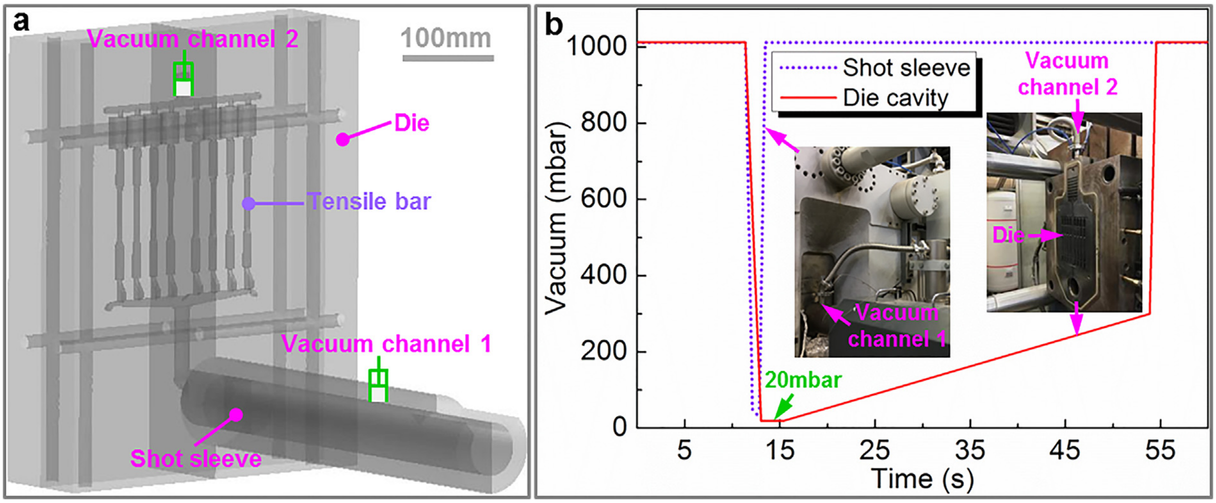

Fig. 1. The frontier two-stage super vacuum assisted high pressure die casting process used for the fabrication of the die-cast AlSiMgMn–TiB_2 composites. (a) Schematic showing the ASTM B557 standard round tensile test bars of the composites casted under the super vacuum assisted die casting process, (b) Vacuum curves showing the frontier 20 mbar super vacuum achieved during the die casting process.

TiB_2 nanoparticle in Fig. 2b, and Fig. 2d shows the HRTEM image of the TiB_2 nanoparticle in Fig. 2b, which verified that the nanoparticles dispersed in the Al–10wt.%TiB_2 master alloy were TiB_2.

The TiB_2 nanoparticles were in the morphology of hexagonal prisms with hexagonal close packed lattice structure, and the faceted morphology of the TiB_2 nanoparticles observed here agreed with the previous report [34,35]. The size of the TiB_2 nanoparticles under the in-situ reaction was well reported showing a log-normal distribution in the range of 0–450 nm with the majority of the TiB_2 nanoparticles between 50 and 125 nm, while the average diameter of the TiB_2 nanoparticles was ~100 nm [36], which was in consistence with the TiB_2 nanoparticles synthesized here. The TiB_2 nanoparticles are ceramic phases with a high melting point of 3230 °C, and the TiB_2 nanoparticles are stable phases that don't react with molten Al after the formation through in-situ reaction. Moreover, it is easier to add the TiB_2 nanoparticles into the Al melts through the Al–TiB_2 master alloy rather than the pure TiB_2 powders. Thus, the TiB_2 nanoparticles were added into the die-cast Al–Si–Mg–Mn alloy melts through the in-situ synthesized Al–10wt.%TiB_2 master alloy, for the achieving of high performance die-cast AlSiMgMn–TiB_2 composites.

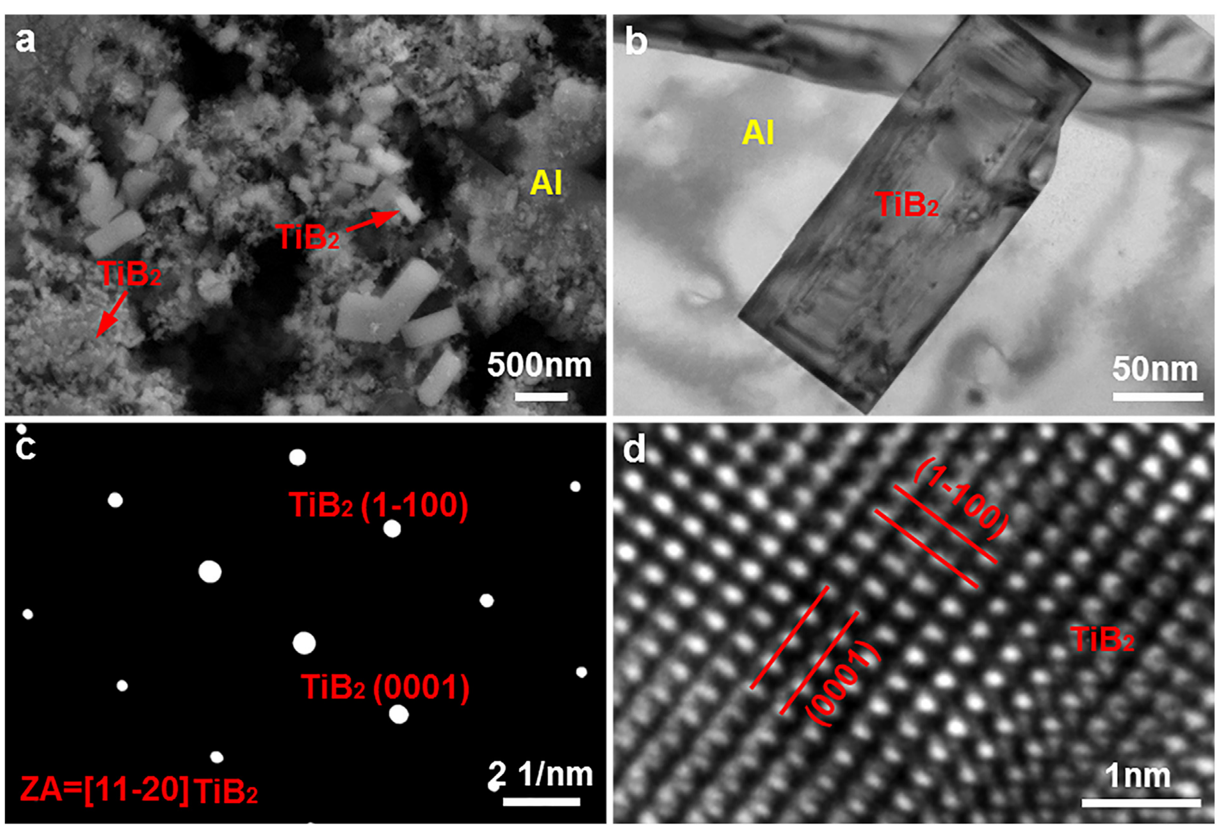

Fig. 2. SEM and TEM micrographs showing the TiB_2 nanoparticles in the Al–10wt.%TiB_2 master alloy. (a) Morphology and distribution of TiB_2 nanoparticles under SEM observation, (b) Bright-field TEM morphology of TiB_2 nanoparticle, (c) SADP and (d) HRTEM image of the TiB_2 nanoparticle in (b).

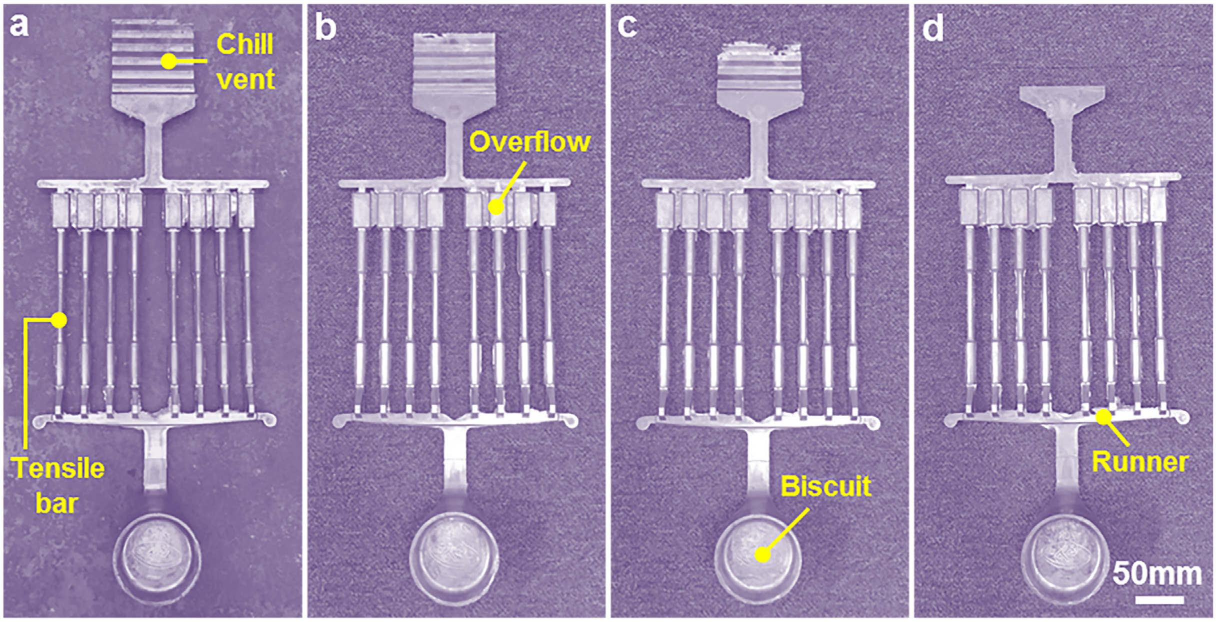

Fig. 3. Castings of the die-cast AlSiMgMn–TiB_2 composites fabricated under the frontier super vacuum assisted high pressure die casting. (a) 0 wt% TiB_2 reinforced alloy, (b) 1.5 wt% TiB_2 reinforced composite, (c) 3.5 wt% TiB_2 reinforced composite, (d) 4.5 wt% TiB_2 reinforced composite.

3.2. As-cast AlSiMgMn–TiB_2 composites

3.2.1. Casting and die-cast capability

Fig. 3 shows the castings of the AlSiMgMn–TiB_2 composites fabricated under the super vacuum assisted HPDC. Fig. 3a presents the casting of the AlSiMgMn die-cast alloy without TiB_2 reinforcement, and the casting was well filled with high integrity and no hot-tearing crack, indicating the excellent die-cast capability of the base alloy. Fig. 3b shows the casting of the 1.5 wt% TiB_2 reinforced composite, and the integrity of the casting was similar to that of the base alloy, indicative of the good die-cast capability of the AlSiMgMn–1.5 wt% TiB_2 composite. Fig. 3c presents the casting of the 3.5 wt% TiB_2 reinforced composite, and the casting was still well filled to the thin (0.8 mm thickness) chill vent end with good integrity and no hot-tearing crack, indicating the

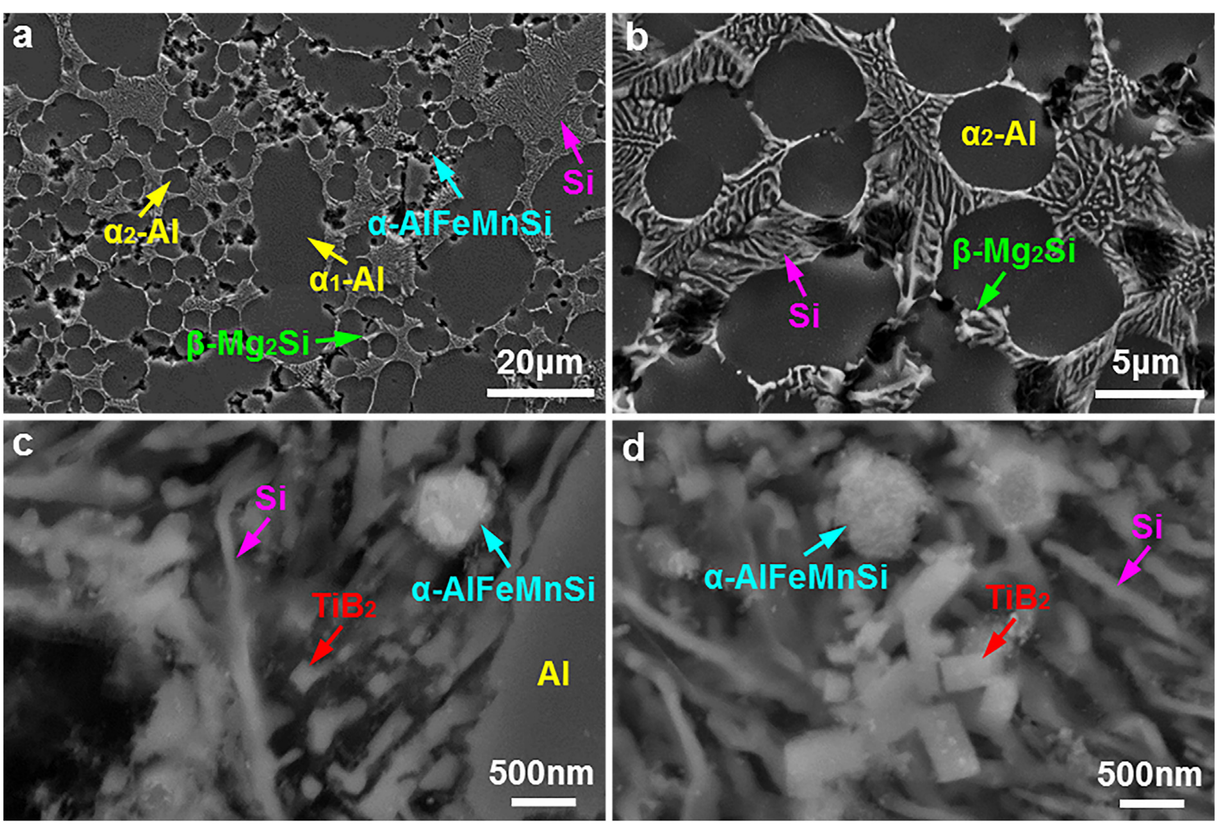

Fig. 4. SEM micrographs showing the microstructure of the die-cast AlSiMgMn–TiB_2 composites in as-cast state. (a, b) 0 wt% TiB_2 reinforced alloy, (c) 1.5 wt% TiB_2 reinforced composite, (d) 3.5 wt% TiB_2 reinforced composite.

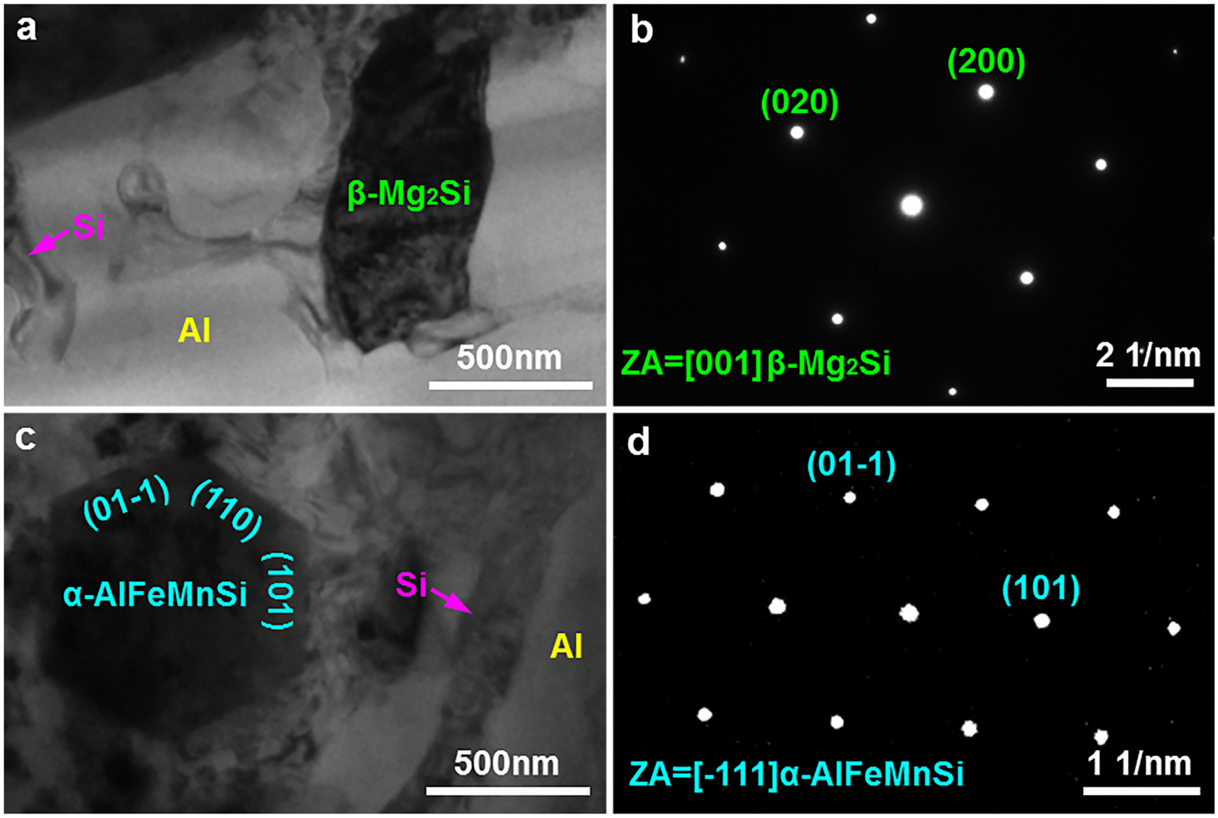

Fig. 5. TEM micrographs confirming the intermetallic phases in the die-cast AlSiMgMn–TiB_2 composites in as-cast state. (a) Bright-field TEM image of the β–Mg_2Si intermetallic phase, (b) SADP of the β–Mg_2Si intermetallic phase in (a), (c) Bright-field TEM image of the α–AlFeMnSi intermetallic phase, (d) SADP of the α–AlFeMnSi intermetallic phase in (c).

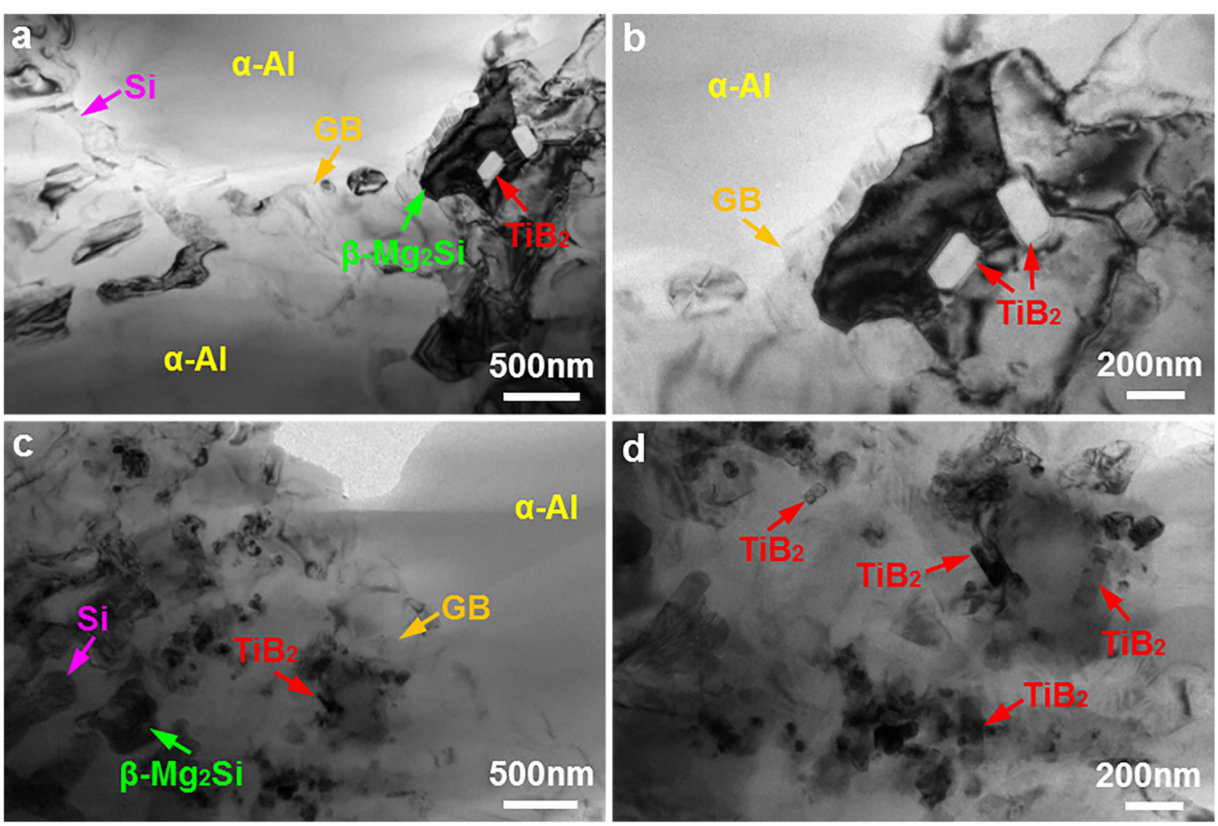

Fig. 6. Bright-field TEM micrographs showing the distribution of the TiB_2 nanoparticles in the die-cast AlSiMgMn–TiB_2 composites in as-cast state. (a) 1.5 wt% TiB_2 reinforced composite, (b) Enlarged morphology of the TiB_2 nanoparticles at the grain boundary (GB) in (a), (c) 3.5 wt% TiB_2 reinforced composite, (d) Enlarged morphology of the TiB_2 nanoparticles at the grain boundary in (c).

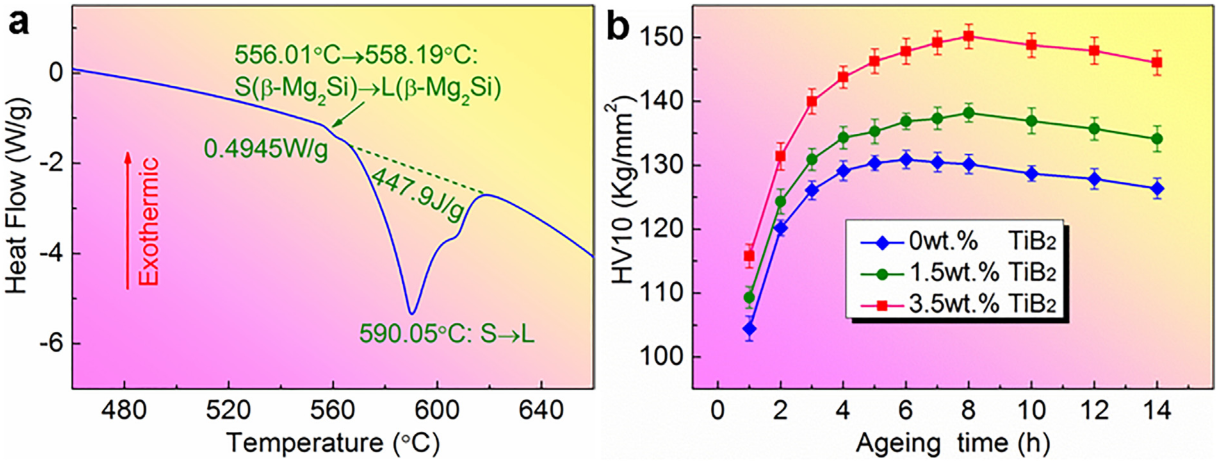

Fig. 7. (a) DSC thermal analysis result showing the solid-liquid transition temperature of the β-Mg_2Si intermetallic phase in the die-cast AlSiMgMn–TiB_2 composites, (b) Evolution of the hardness of the die-cast AlSiMgMn–TiB_2 composites versus ageing time after solution treatment.

good die-cast capability of the AlSiMgMn–3.5 wt% TiB_2 composite. Fig. 3d shows the casting of the 4.5 wt% TiB_2 reinforced composite, and the casting could not be filled to the chill vent end, indicative of the poor die filling capability of the alloy melt with 4.5 wt% TiB_2. Comparing with the base alloy, the decrease of the chill vent height in the castings of the composites was due to the decrease of the fluidity of the alloy melts after addition of TiB_2 nanoparticles. The high content of silicon ensured the excellent fluidity and the low solidification temperature range and thermal expansion of the base alloy, and this led to the excellent die castability of the base alloy. The die castability of the composites was good within the addition of 3.5 wt% TiB_2, due to the excellence of the die castability of the base alloy. The composite with 4.5 wt% TiB_2 or above was not suitable for HPDC due to the significant decrease of the die filling capability.

3.2.2. As-cast microstructure

Fig. 4a and b present the SEM morphology of the as-cast AlSiMgMn die-cast alloy without TiB_2 reinforcement. The microstructure of the

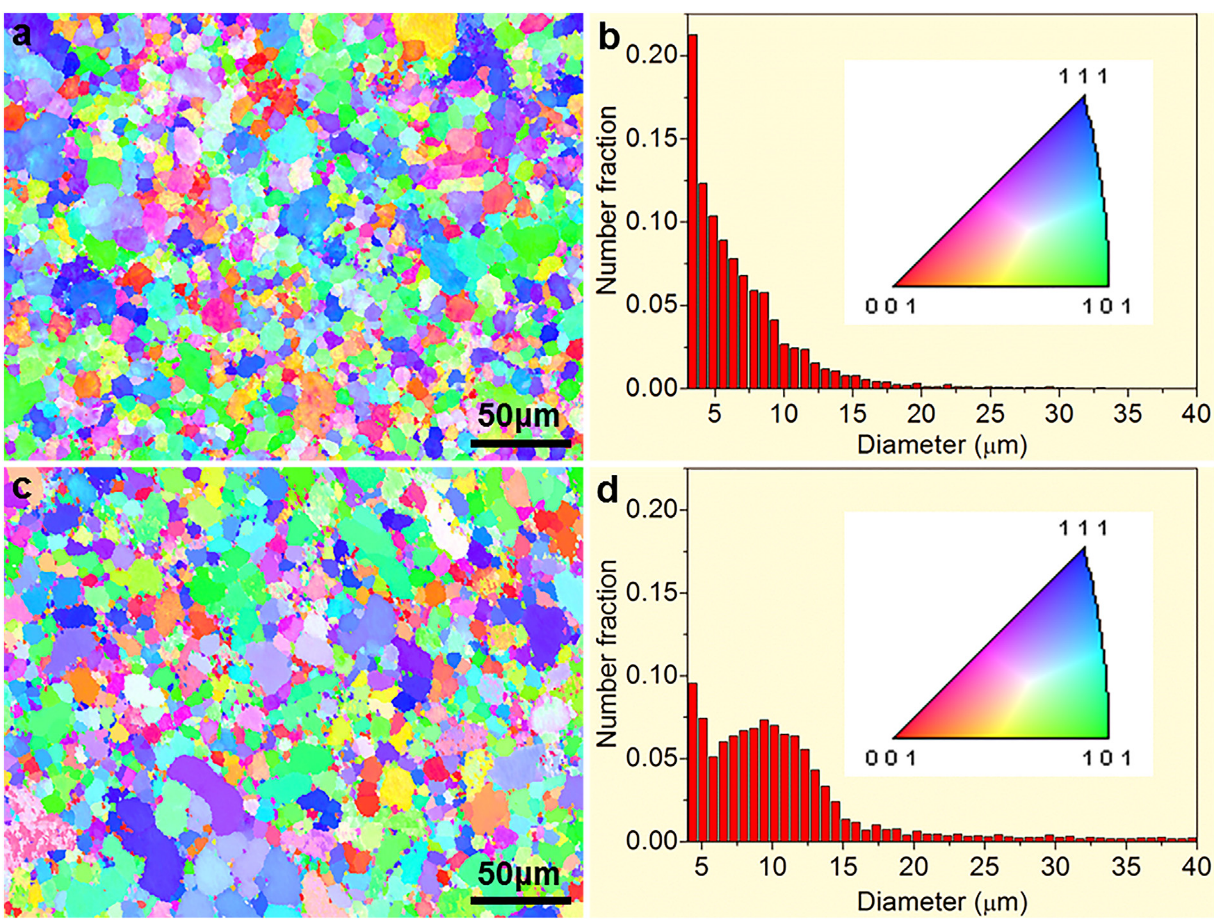

Fig. 8. EBSD results showing the evolution of the α–Al phase in the die-cast AlSiMgMn–TiB_2 composites during T6 heat treatment. (a) IPF orientation map and (b) grain size distribution of the α–Al phase in the 3.5 wt% TiB_2 reinforced composite in as-cast state, (c) IPF orientation map and (d) grain size distribution of the α–Al phase in the 3.5 wt% TiB_2 reinforced composite after T6 heat treatment.

alloy comprised the α–Al phase, the eutectic Si phase and the intermetallic phases of α–AlFeMnSi and β–Mg_2Si. The α–Al phase was in two different sizes, i.e., the relatively coarse primary α_1–Al phase solidified in the shot sleeve with lower cooling rate and the fine secondary α_2–Al phase solidified in the die cavity with higher cooling rate. The eutectic Si phase was in fibrous morphology due to the modification effect of the element Sr [37–39]. The β–Mg_2Si intermetallic phase distributed at the grain boundary of the α–Al phase, and it was in block shape. Fig. 4c shows the SEM morphology of the as-cast AlSiMgMn–1.5 wt% TiB_2 composite, TiB_2 nanoparticles were observed in the eutectic area that was at the grain boundary. The eutectic Si phase was also in fibrous morphology, and the α–AlFeMnSi intermetallic phase was in faceted morphology. Fig. 4d presents the SEM morphology of the as-cast AlSiMgMn–3.5 wt% TiB_2 composite, TiB_2 nanoparticles were also observed in the eutectic area that was at the grain boundary, and the amount of the TiB_2 nanoparticles at the grain boundary of the 3.5 wt% TiB_2 reinforced composite was higher than that of the 1.5 wt% TiB_2 reinforced composite. The size of the faceted α–AlFeMnSi intermetallic phase was ~0.5–1 μm.

The intermetallic phase of β was rich in Mg and Si, and the intermetallic phase of α– AlFeMnSi was rich in Al, Fe, Mn and Si, according to the energy dispersive X-ray spectroscopy (EDS) analysis under SEM. However, it was hard to determine the chemical formula and structure of the intermetallic phases under SEM, as the measurement accuracy of the element content was not high enough. Therefore, TEM analysis was applied to confirm the β and α–AlFeMnSi intermetallic phases in the as-fabricated composites. Fig. 5a shows the bright-field TEM morphology of the β phase, and the SADP analysis result in Fig. 5b verified that the β phase was the Mg_2Si phase with the face centred cubic lattice structure. The lattice parameter of the β phase was determined as 0.638 nm from the (200) interplanar spacing of 0.319 nm measured in Fig. 5b, which agreed well with the reported lattice parameter of 0.639 nm of the β–Mg_2Si phase [40]. Fig. 5c presents the bright-field TEM morphology of the α– AlFeMnSi phase, and the SADP analysis result in Fig. 5d confirmed that the α–AlFeMnSi phase was the $Al_{15}(Fe,Mn)_3Si_2$ phase with the body centred cubic lattice structure. The lattice parameter of the α–AlFeMnSi phase was determined as 1.270 nm from the (0−11) interplanar spacing of 0.898 nm measured in Fig. 5d, which agreed well with the reported lattice parameter of 1.270 nm of the $Al_{15}(Fe,Mn)_3Si_2$ phase [41].

Fig. 6 presents the bright-field TEM micrographs showing the distribution of the TiB_2 nanoparticles in the die-cast AlSiMgMn–TiB_2 composites in as-cast state. Fig. 6a and b show the TEM morphology of the 1.5 wt% TiB_2 reinforced composite in as-cast state, and the TiB_2 nanoparticles were found distributing at the grain boundary (GB) of the α–Al phase. The matrix of the α–Al phase was clean, and hardly did the TiB_2 nanoparticles present in the α–Al grain. Fig. 6c and d present the TEM morphology of the 3.5 wt% TiB_2 reinforced composite in as-cast state, and the TiB_2 nanoparticles were also observed distributing at the grain boundary of the α–Al phase rather than in the α–Al grain. The amount of the TiB_2 nanoparticles at the grain boundary of the 3.5 wt% TiB_2 reinforced composite was higher than of the 1.5 wt% TiB_2 reinforced composite, due to the increased addition of the TiB_2 nanoparticles. The distribution of the TiB_2 reinforcement nanoparticles at the grain boundary of the α–Al phase rather than in the α–Al matrix was also reported in the laser additive manufacturing of the nano-TiB_2 decorated AlSi10Mg aluminium alloy [42], which had the cooling rate that was three orders of magnitude (10^3) higher than the present HPDC (500–1000 K/s) process.

3.3. Heat treatment of AlSiMgMn–TiB_2 composites

3.3.1. Heat treatment process

The micron-scale β–Mg_2Si intermetallic phase at the grain boundary was expected dissolving into the α–Al matrix during solution treatment, and precipitating out in the form of nanoscale precipitates in the α–Al matrix during the subsequent ageing treatment, for the heat

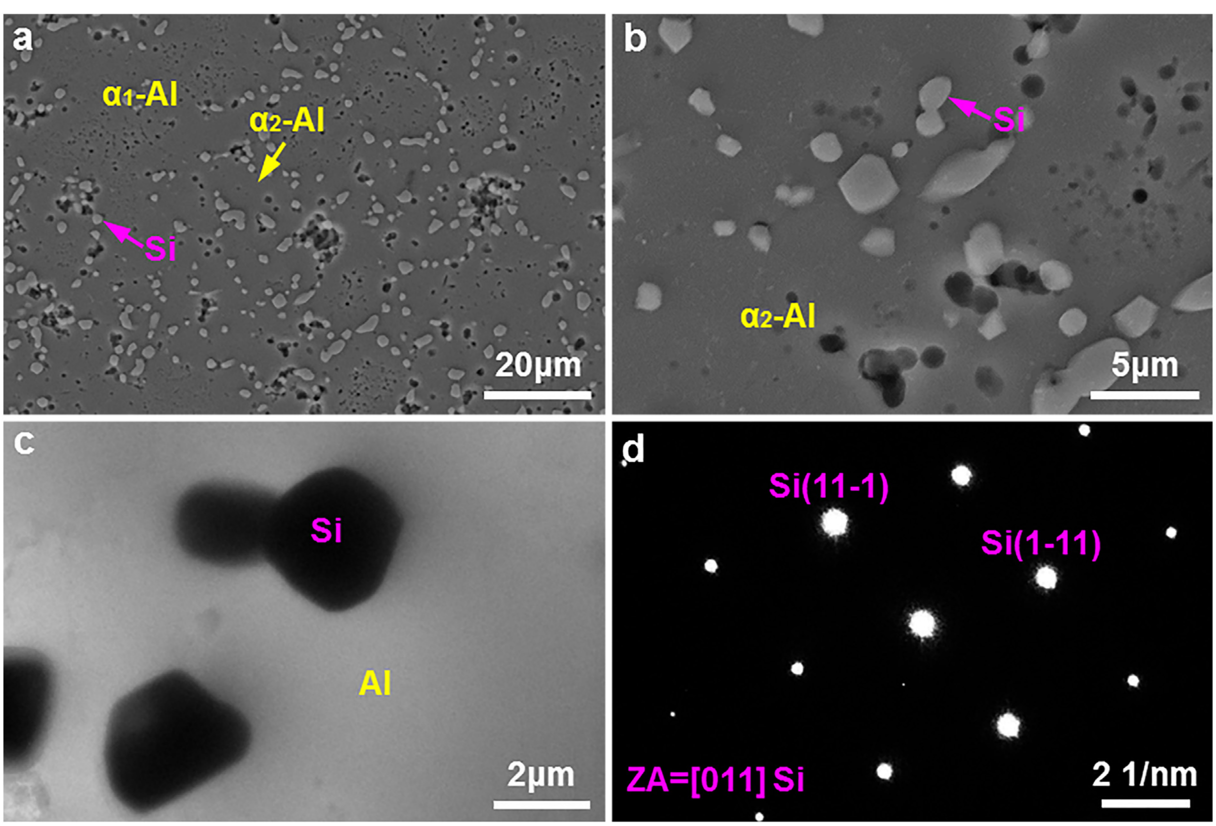

Fig. 9. SEM and TEM micrographs showing the microstructure of the die-cast AlSiMgMn alloy after solution treatment. (a) Low magnification SEM morphology, (b) Enlarged SEM morphology, (c) Bright-field TEM morphology of the spheroidized Si phase, (d) SADP of the Si phase in (c).

treatment strengthening of the die-cast AlSiMgMn–TiB_2 composites. The melting temperature of the β intermetallic phase was determined as 557.1 °C by DSC analysis, as shown in Fig. 7a, and the solid solution temperature was therefore chosen as 540 °C. Fig. 7b shows the evolution of the hardness of the die-cast AlSiMgMn–TiB_2 composites versus ageing time after solution treatment. With the increase of the ageing time, the hardness first increased till reached the peak due to the precipitation of the fine nanoscale precipitates, and decreased subsequently resulting from the transformation of the fine nanoscale precipitates into the relatively coarser nanoscale precipitates. The fine nanoscale precipitates are highly coherent with the Al matrix and have strong precipitation strengthening effect, while the coarsened nanoscale precipitates are not fully coherent with the Al matrix and have relatively weaker precipitation strengthening effect. The hardness of the 0 wt% TiB_2 reinforced alloy reached the peak at the ageing time of 6 h, while the hardness of the 1.5 wt% TiB_2 and 3.5 wt% TiB_2 reinforced composites reached the peak at the ageing time of 8 h. The hardness of the heat-treated composites increased with increasing content of TiB_2, and the peak hardness of the 3.5 wt% TiB_2 reinforced composite was as high as 150.2 kg/mm^2. The peak ageing hours of 6 h, 8 h and 8 h were chosen as the final ageing time of T6 heat treatment for the 0 wt% TiB_2, 1.5 wt % TiB_2 and 3.5 wt% TiB_2 reinforced composites, separately.

3.3.2. Evolution of the α–Al matrix phase

Fig. 8 presents the evolution of the α–Al phase in the die-cast AlSiMgMn–TiB_2 composites during T6 heat treatment by EBSD analysis. Fig. 8a shows the inverse pole figure (IPF) orientation map of the α–Al phases in the 3.5 wt% TiB_2 reinforced composite in as-cast state, and the insert of the colour code in Fig. 8b represents the detail crystal orientation of the α–Al phases in Fig. 8a. Different α–Al phases can be easily distinguished by the difference of the orientation colour under IPF. Fig. 8b presents the grain size distribution of the α–Al in the as-cast composite, the α_1–Al could be large as 30 μm, while the α_2–Al could be small as 3 μm. Fig. 8c shows the IPF orientation map of the α–Al phases in the 3.5 wt% TiB_2 reinforced composite after T6 heat treatment. The grain size of the α–Al phase in Fig. 8c was obviously coarser than that in Fig. 8a, which indicated that the α–Al phase was coarsened during T6 heat treatment. Fig. 8d presents the grain size distribution of the α–Al phase in the 3.5 wt% TiB_2 reinforced composite after T6 heat treatment, and it also verified the coarsening of the α–Al phase during T6 heat treatment, as the α–Al phase was shifted to direction of larger grain size. The combining of the neighbouring α–Al grains during the high temperature solution treatment at 540 °C led to the coarsening of the α–Al phase by diffusion.

3.3.3. Evolution of the eutectic and intermetallic phases

Fig. 9a and b show the SEM morphology of the die-cast AlSiMgMn alloy after solution treatment. The fibrous eutectic Si phase in the as-cast alloy was spheroidized into the fine spheroidal Si particles after solution treatment. The β intermetallic phase was hardly observed in the solution treated alloy, which indicated that the β phase at the grain boundary of the as-cast alloy was well dissolved into the α–Al matrix after solution treatment. Fig. 9c presents the bright-field TEM morphology of the die-cast AlSiMgMn alloy after solution treatment, and the SADP in Fig. 9d verified that the spheroidized particle in Fig. 9c was the Si phase. The lattice parameter of the Si phase was determined as 0.544 nm from the (111) interplanar spacing of 0.314 nm measured in Fig. 9d, which agreed well with the lattice parameter of 0.543 nm of

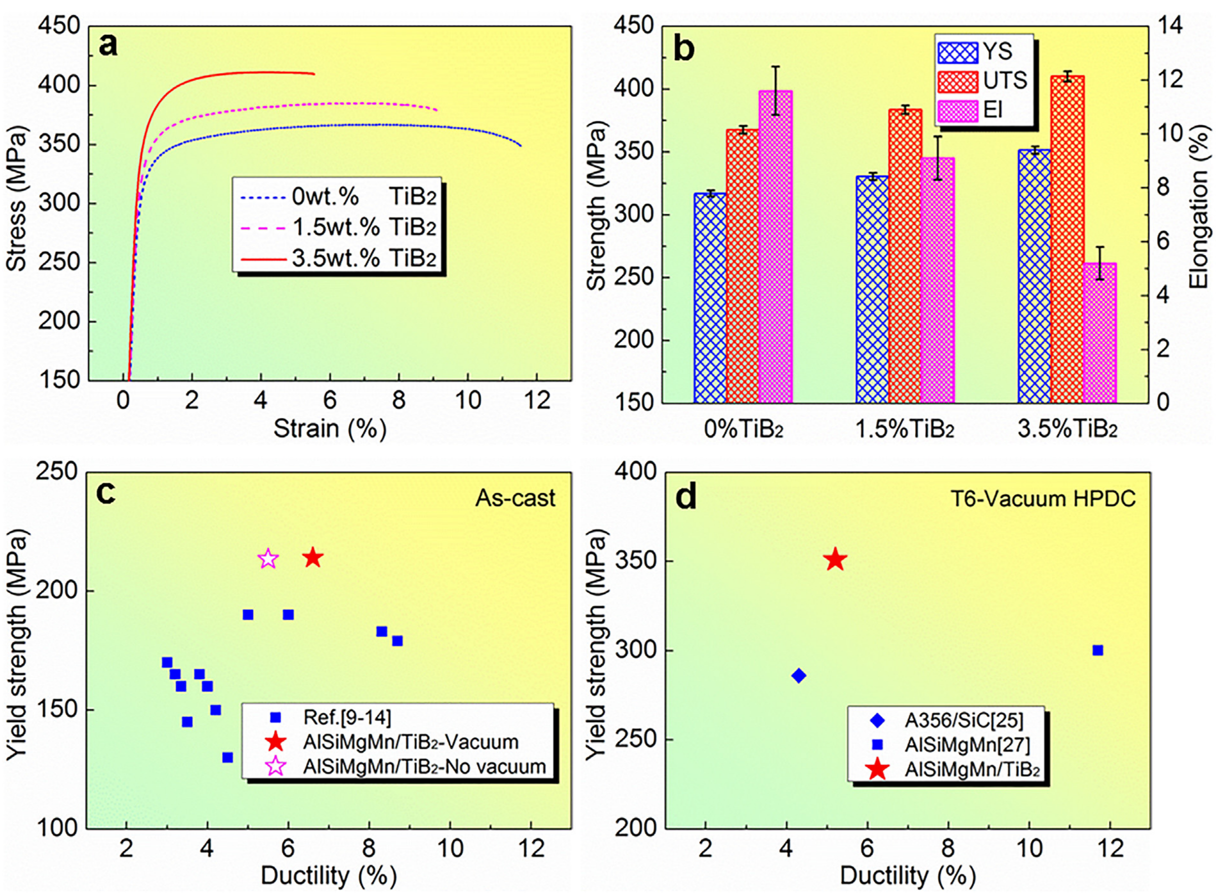

Fig. 10. Tensile properties of the die-cast AlSiMgMn–TiB_2 composites. (a) Typical tensile stress-strain curves and (b) average tensile properties of the T6 heat-treated composites under super vacuum assisted HPDC, (c) As-cast tensile properties of the 3.5 wt% TiB_2 reinforced composite under non-vacuum and vacuum assisted HPDC and comparison with reference as-cast tensile properties [9–14], (d) T6 heat treated tensile properties of the 3.5 wt% TiB_2 reinforced composite under vacuum assisted HPDC and comparison with reference T6 heat treated tensile properties under vacuum assisted HPDC [25,27].

the Si phase with diamond cubic structure. The spheroidization of the eutectic Si phase during solution treatment was also reported by previous studies on Al—Si based cast alloys [43–45], and the dissolving of the β phase into the α–Al matrix was due to the high temperature diffusion during solution treatment.

3.4. Heat-treated AlSiMgMn–TiB_2 composites

3.4.1. Tensile properties

Fig. 10a presents the typical tensile stress-strain curves of the T6 heat-treated die-cast AlSiMgMn–TiB_2 composites under super vacuum assisted HPDC. With the increase of TiB_2 nanoparticles, the strength of the T6 heat-treated composites increased, while the ductility decreased. Fig. 10b shows the average tensile properties of the T6 heat-treated die-cast AlSiMgMn–TiB_2 composites under super vacuum assisted HPDC. The yield strength, ultimate tensile strength (UTS) and elongation (El) of the 0 wt% TiB_2 reinforced alloy were 317 ± 2 MPa, 368 ± 3 MPa and 11.6 ± 0.9%, respectively. The 1.5 wt% TiB_2 reinforced composite provided the yield strength of 330 ± 3 MPa and UTS of 384 ± 3 MPa in conjunction with the ductility of 9.1 ± 0.8%, and the 3.5 wt% TiB_2 reinforced composite delivered the high yield strength of 351 ± 3 MPa and UTS of 410 ± 4 MPa in association with the good ductility of 5.2 ± 0.6%. Fig. 10c presents the as-cast tensile properties of the 3.5 wt% TiB_2 reinforced composite under non-vacuum and super vacuum assisted HPDC. Compared with non-vacuum assisted HPDC, super vacuum assisted HPDC could improve the ductility of the composite, while it could not improve the yield strength of the composite, which agreed with previous study [27]. The ductility of the as-cast 3.5 wt% TiB_2 reinforced composite was 5.5% under non-vacuum assisted HPDC, while the ductility of the composite improved to 6.6% under super vacuum assisted HPDC. The as-cast yield strength of the 3.5 wt% TiB_2 reinforced composite was 214 MPa, and it was at least 25 MPa higher than the as-cast yield strength of the currently available die-cast aluminium alloys [9–14]. The T6 heat-treated composite reinforced

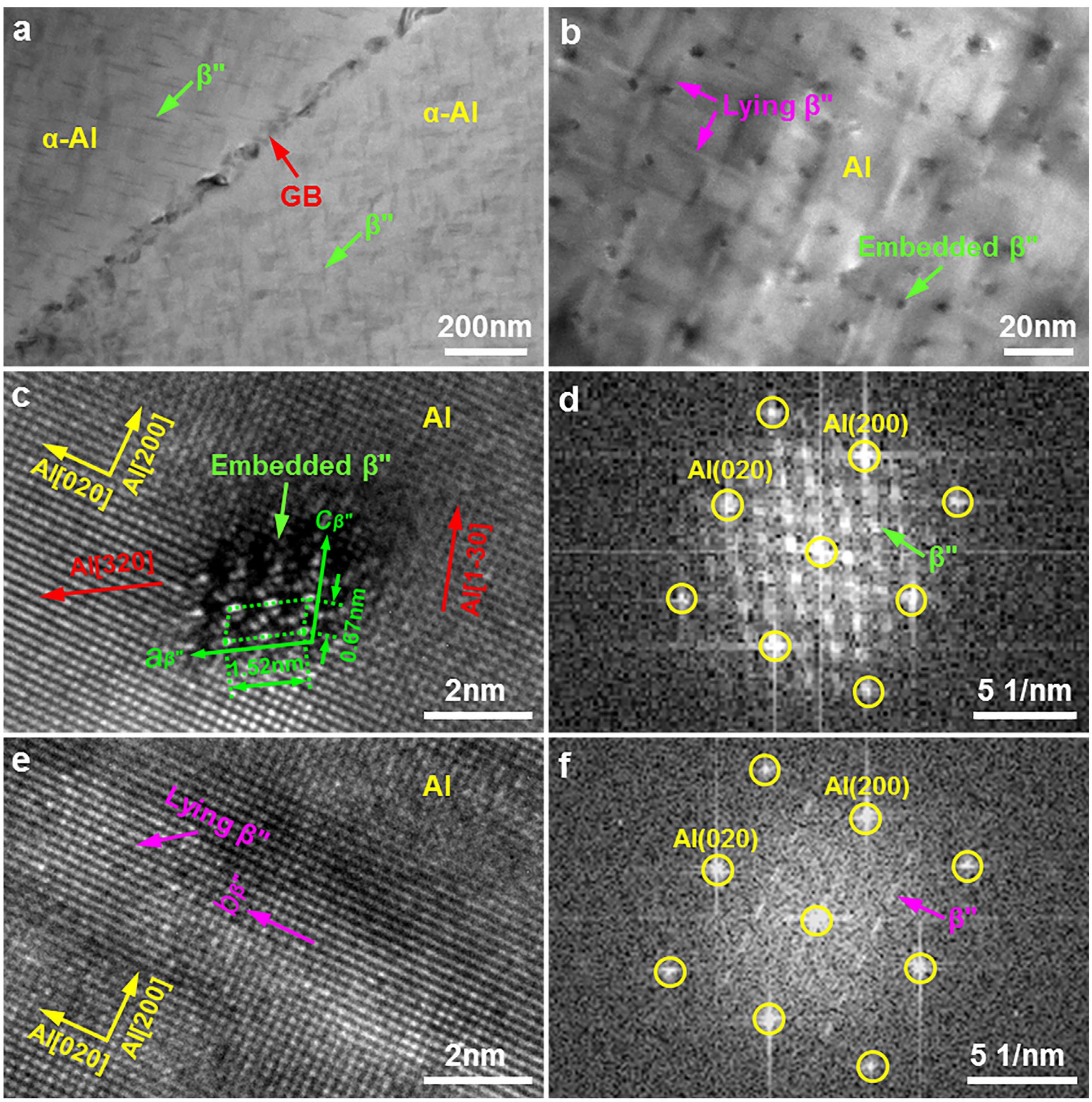

Fig. 11. TEM micrographs showing the nanoscale β″ precipitates in the Al matrix of the die-cast AlSiMgMn alloy after T6 heat treatment. (a) Bright-field image taken from non-zone axis of Al, (b) Bright-field image taken along the ⟨001⟩ zone axis of Al, (c) HRTEM image of embedded β″ precipitate in (b), (d) FFT pattern of (c), (e) HRTEM image of lying β″ precipitate in (b), (f) FFT pattern of (e).

by 3.5 wt% TiB_2 demonstrated 17% increase in yield strength over the previously reported [27] T6 heat-treated die-cast AlSiMgMn alloy without particle reinforcement, and it also demonstrated 23% increase in yield strength over the T6 heat-treated A356 Al alloy reinforced by SiC particles [25], under vacuum assisted HPDC, as shown in Fig. 10d. It is hard to achieve die-cast aluminium alloys with the high yield strength of 350 MPa in association with an industrially applicable ductility of 4%. The high mechanical performances delivered by the AlSiMgMn–3.5wt%TiB_2 composite are excellent mechanical properties for the HPDC industry.

3.4.2. Precipitation strengthening

The TEM images in Fig. 11 show the nanoscale precipitates in the α–Al matrix of the present die-cast alloy after T6 heat treatment. Fig. 11a presents the bright-field TEM image taken along the non-zone axis of the α–Al matrix, and nanoscale β″–Mg_2Si precipitates dispersed homogeneously in the matrix of different α–Al phases. Fig. 11b shows the bright-field TEM image taken along the <001> zone axis of one α–Al grain, and embedded and lying β″ nanoscale precipitates dispersed uniformly in the α–Al matrix. The β″ precipitate was in needle-like shape [40], and the embedded and lying β″ precipitates were the same β″ precipitates. Fig. 11c presents the HRTEM image of the embedded β″ precipitate, and it clearly presented the unit cell of C-centered monoclinic structure with a = 1.52 nm and c = 0.67 nm, which verified that the embedded precipitate was β″ [40,46], and the nanoscale β″ precipitate was coherent with the α–Al matrix with Al[320]//β″(a-axis) and Al[1-30]//β″(c-axis). The fast Fourier transform (FFT) pattern in Fig. 11d also confirmed that the embedded precipitate in Fig. 11c was β″. Fig. 11e shows the HRTEM image of the lying β″ precipitate, which had coherent interface with the α–Al matrix with Al[020]//β″(b-axis). The FFT pattern in Fig. 11f verified that the lying precipitate in Fig. 11e was β″ [43]. The coherence between β″ precipitate and the Al matrix led to excellent precipitation strengthening of the Al matrix.

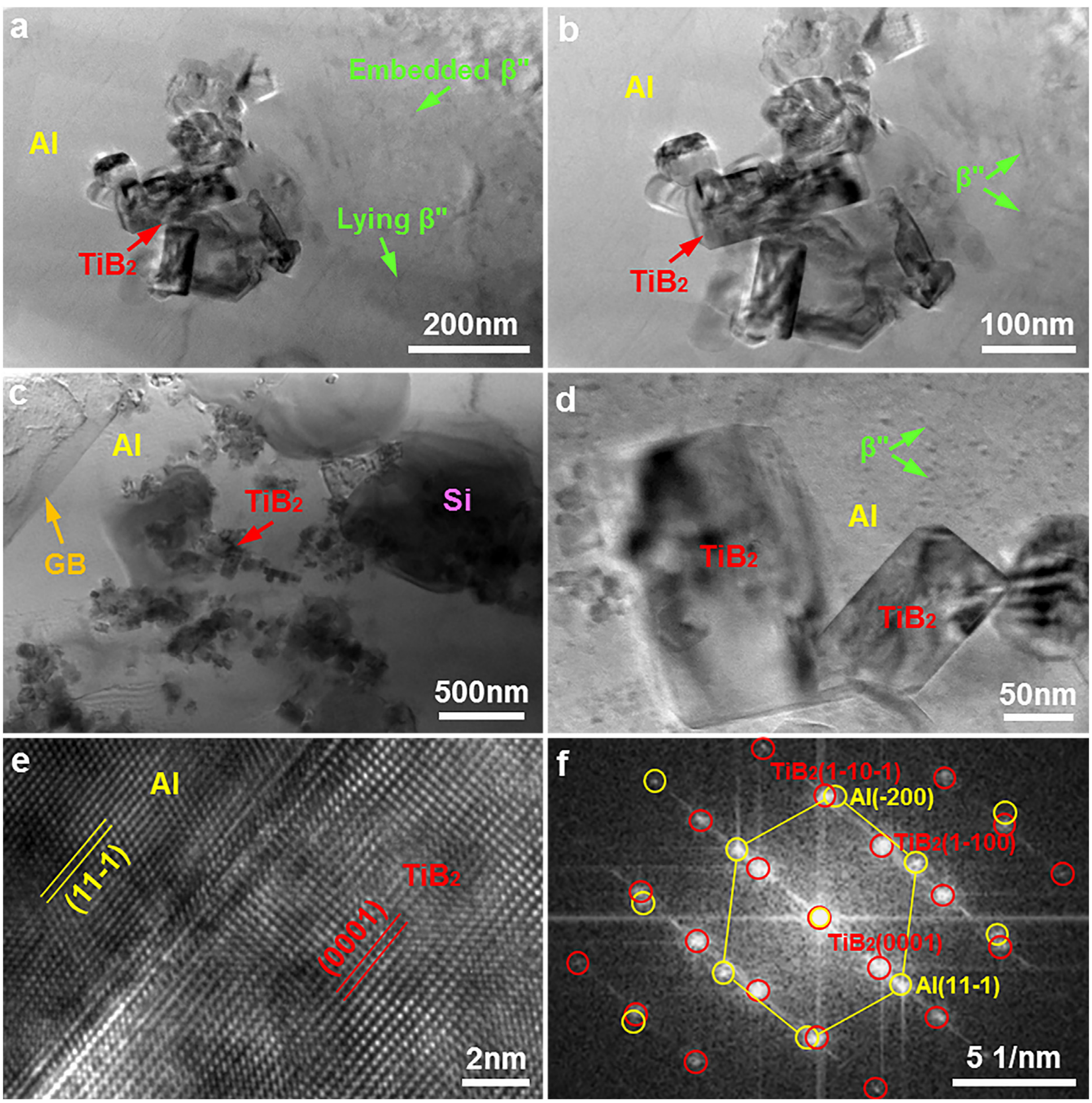

Fig. 12. TEM micrographs showing the TiB_2 nanoparticles and the nanoscale β″ precipitates a in the Al matrix of the die-cast AlSiMgMn–TiB_2 composites after T6 heat treatment. Bright-field images of the (a, b) 1.5 wt% and (c,d) 3.5 wt% TiB_2 reinforced composites, (e) HRTEM image and (f) FFT pattern showing the interface and orientation relation between the middle TiB_2 nanoparticle and the Al matrix in (d).

3.4.3. Nanoparticle strengthening

Fig. 12 presents the TEM micrographs of the die-cast AlSiMgMn–TiB_2 composites after T6 heat treatment. Fig. 12a and b show the bright-field TEM images of the α–Al matrix of the 1.5 wt% TiB_2 reinforced composite, and the strengthening of the α–Al matrix was a result of both β″ precipitates and TiB_2 nanoparticles. Fig. 12c and d present the bright-field TEM images of the α–Al matrix of the 3.5 wt% TiB_2 reinforced composite, and the strengthening of the α–Al matrix of the composite was also a result of both β″ precipitates and TiB_2 nanoparticles. The number density of the nanoscale β″ precipitates in Fig. 12 seemed lower than that in Fig. 11, which was due to the difference of the observing direction under TEM, and the number density of the nanoscale β″ precipitates in the 0 wt%, 1.5 wt% and 3.5 wt% TiB_2 reinforced composites was identical. From Fig. 6, the TiB_2 nanoparticles distributed at the grain boundary rather than in the α–Al matrix of the composites in as-cast state. As verified by the EBSD analysis in Fig. 8, the nearby α–Al phases in as-cast state were combined and coarsened during the subsequent solution treatment. The TiB_2 nanoparticles at the grain boundaries of the as-cast composite were therefore enrolled into the α–Al matrix of T6 heat-treated composite through the combining and coarsening of the α–Al phases during the solution treatment. Fig. 12e presents the HRTEM image showing the interface between the middle TiB_2 nanoparticle and the α–Al matrix in Fig. 12d, and the TiB_2 nanoparticle was found having highly coherent interface with the α–Al matrix, with the (0001) crystal plane of the TiB_2 nanoparticle parallel to the (11−1) crystal plane of the α–Al matrix, which indicated strong interfacial bonding and strengthening. The FFT pattern in Fig. 12f revealed that the crystal orientation relation (OR) between the TiB_2 nanoparticle and the α–Al matrix was Al(11-1)//TiB_2(0001) and Al[011]//TiB_2[11-20]. Thus the strengthening of the present die-cast AlSiMgMn–TiB_2 composites was a result of both TiB_2 nanoparticles and nanoscale β″ precipitates that had coherent interfaces with the α–Al matrix, which resulted in the high strength of the composites.

3.5. Ductile fracture

Fig. 13 shows the SEM micrographs of the tensile fracture of the die-cast AlSiMgMn–TiB_2 composites after T6 heat treatment. Fig. 13a presents the SEM morphology of the fracture of the 0 wt% TiB_2 reinforced alloy, and Al dimples were found distributing uniformly across the fracture indicating the ductile fracture, which agreed with the excellent ductility of the alloy. Cracks were found in the Si phase due to its brittle feature [37,43]. Fig. 13b shows the SEM morphology of the fracture of the 1.5 wt% TiB_2 reinforced composite, and TiB_2 nanoparticles were observed on the fracture, while cracks were still found in the Si phase. The number of the Al dimples was slightly smaller on the fracture of the 1.5 wt% TiB_2 reinforced composite when compared with the 0 wt% TiB_2 reinforced alloy, and it corresponded to the slight decrease of the ductility of the composite. Fig. 13c and d present the SEM morphology of the fracture of the 3.5 wt% TiB_2 reinforced composite, and it also comprised the Al dimples, the cracked Si phase and the TiB_2 nanoparticles. The number of the Al dimples was decreased on the fracture of the 3.5 wt% TiB_2 reinforced composite, which was in consistence with the decrease of the ductility of the composite. The TiB_2 nanoparticles are hard phases with the super high hardness of 2500 kg/mm^2, and the Si phase is brittle phase with the high hardness of 900 kg/mm^2. With the increased addition of the TiB_2 nanoparticles to 3.5 wt%, the number of the hard TiB_2 nanoparticles surrounding the brittle Si phase increased significantly, as shown in Fig. 13c. It could be reasonably speculated that the brittle Si phase would be inevitably interacted with its surrounding hard TiB_2 nanoparticles, under the loading and deformation of tensile test, which very possibly accelerated the crack of the brittle Si phase and the fracture of the composite. The presence of the Al dimples on the tensile fracture confirmed the ductile fracture [47] and the good ductility of the high strength die-cast AlSiMgMn–3.5wt%TiB_2 composite.

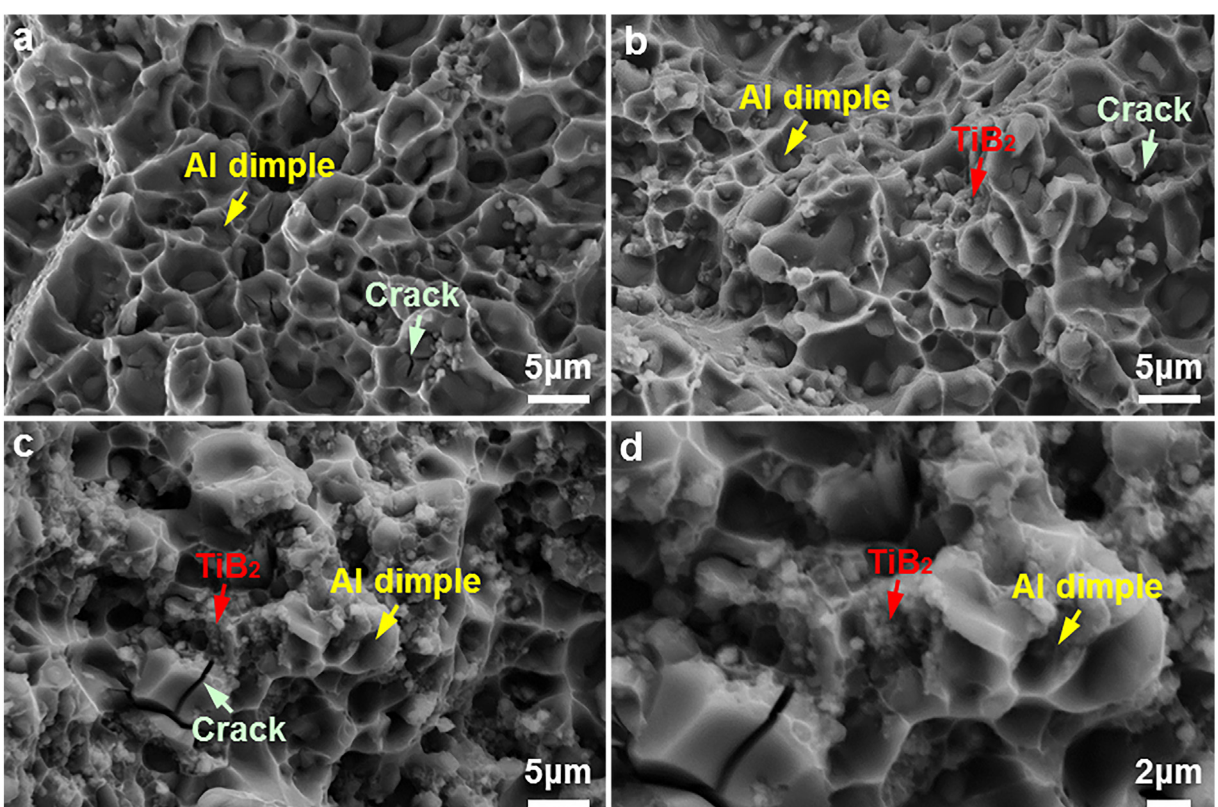

Fig. 13. SEM morphology of the tensile fracture of the die-cast AlSiMgMn–TiB_2 composites after T6 heat treatment. (a) 0 wt% TiB_2 reinforced alloy, (b) 1.5 wt% TiB_2 reinforced composite, (c, d) 3.5 wt% TiB_2 reinforced composite.

4. Conclusions

Die-cast AlSiMgMn–TiB_2 composites with advanced mechanical performance were successfully fabricated, through the implantation of TiB_2 nanoparticles. The super vacuum of 20 mbar was achieved in the die cavity in limited evacuation time of 1.6 s under the super vacuum assisted high pressure die casting, for the fabrication of the composites. The as-fabricated AlSiMgMn–3.5wt%TiB_2 composite could deliver the high hardness of 150.2 kg/mm^2, the high yield strength of 351 MPa and ultimate tensile strength of 410 MPa, and an industrially applicable good ductility of 5.2%, after T6 heat treatment. In addition, the as-fabricated composites demonstrated good die castability within the implantation of 3.5 wt.% TiB_2 nanoparticles. Furthermore, the strengthening of the α–Al matrix of the T6 heat-treated composite was a result of both TiB_2 nanoparticles and nanoscale β″ precipitates that had coherent interfaces with the Al matrix, i.e., Al(11-1)//TiB_2(0001), Al[011]//TiB_2[11-20], Al[320]//β″(*a*-axis), Al[1-30]//β″(*c*-axis) and Al(020)//β″ (*b*-axis), indicative of strong interfacial bonding and strengthening. Moreover, the as-prepared composite showed ductile fracture. The high strength, the industrially applicable ductility, the good die castability and the highly coherent interfacial bonding make the as-fabricated composite promising for applications in industry.

CRediT authorship contribution statement

Xixi Dong: Conceptualization, Methodology, Investigation, Writing - original draft, Writing - review & editing.**Hamza Youssef:** Methodology, Investigation, Writing - original draft.**Yijie Zhang:** Methodology, Investigation.**Hailin Yang:** Investigation.**Shihao Wang:** Investigation. **Shouxun Ji:** Conceptualization, Writing - review & editing, Supervision.

Acknowledgements

The authors gratefully acknowledge the financial support from Innovate UK and National Natural Science Foundation of China with no. 51404302.

Data availability

The raw/processed data required to reproduce the findings cannot be shared at this time as the data also forms part of an ongoing study. However, the data that support the findings of this paper are available from the corresponding author on reasonable request.

Declaration of competing interest

The authors declare no competing interests for the manuscript “Advanced heat treated die-cast aluminium composites fabricated by TiB_2 nanoparticle implantation” submitted to *Materials & Design*.

References

[1] L. Wang, M. Makhlouf, D. Apelian, Aluminium die casting alloys: alloy composition, microstructure, and properties-performance relationships, Int. Mater. Rev. 40 (1995) 221–238.
[2] X.X. Dong, X.S. Huang, L.H. Liu, L.J. He, P.J. Li, A liquid aluminum alloy electromagnetic transport process for high pressure die casting, J. Mater. Process. Technol. 234 (2016) 217–227.
[3] N. Mo, Q.Y. Tan, M. Bermingham, Y.D. Huang, H. Dieringa, N. Hort, M.X. Zhang, Current development of creep-resistant magnesium cast alloys: a review, Mater. Des. 155 (2018) 422–442.
[4] X.X. Dong, G.B. Mi, L.J. He, P.J. Li, 3D simulation of plane induction electromagnetic pump for the supply of liquid Al-Si alloys during casting, J. Mater. Process. Technol. 213 (2013) 1426–1432.
[5] L. Stemper, B. Mitas, T. Kremmer, S. Otterbach, P.J. Uggowitzer, S. Pogatscher, Age-hardening of high pressure die casting AlMg alloys with Zn and combined Zn and Cu additions, Mater. Des. 181 (2019)(UNSP 107927).
[6] X.X. Dong, L.J. He, X.S. Huang, P.J. Li, Coupling analysis of the electromagnetic transport of liquid aluminum alloy during casting, J. Mater. Process. Technol. 222 (2015) 197–205.
[7] X.X. Dong, L.J. He, X.S. Huang, P.J. Li, Effect of electromagnetic transport process on the improvement of hydrogen porosity in A380 aluminum alloy, Int. J. Hydrog. Energy 40 (2015) 9287–9297.
[8] S. Cecchel, D. Ferrario, A. Panvini, G. Cornacchia, Lightweight of a cross beam for commercial vehicles: development, testing and validation, Mater. Des. 149 (2018) 122–134.
[9] Annual Book of ASTM Standardsvol. 02.02, 1993 Warrendale PA, USA.
[10] Y. Zhang, J.B. Patel, J. Lazaro-Nebreda, Z. Fan, Improved defect control and mechanical property variation in high-pressure die casting of A380 alloy by high shear melt conditioning, JOM 70 (2018) 2726–2730.
[11] Z.Q. Hu, L. Wan, S.S. Wu, H. Wu, X.Q. Liu, Microstructure and mechanical properties of high strength die-casting Al–Mg–Si–Mn alloy, Mater. Des. 46 (2013) 451–456.
[12] P. Zhang, Z.M. Li, B.L. Liu, W.J. Ding, Effect of chemical compositions on tensile behaviors of high pressure die-casting alloys Al-10Si-yCu-xMn-zFe, Mater. Sci. Eng. A 661 (2016) 198–210.
[13] X.Z. Zhu, P. Blake, K. Dou, S. Ji, Strengthening die-cast Al-Mg and Al-Mg-Mn alloys with Fe as a beneficial element, Mater. Sci. Eng. A 732 (2018) 240–250.
[14] L.Y. Yuan, L.M. Peng, J.Y. Han, B.L. Liu, Y.J. Wu, J. Chen, Effect of Cu addition on microstructures and tensile properties of high-pressure die-casting Al-5.5Mg-0.7Mn alloy, J. Mater. Sci. Technol. 35 (2019) 1017–1026.
[15] J.P. Oliveira, J.F. Duarte, P. Inacio, N. Schell, R.M. Miranda, T.G. Santos, Production of Al/NiTi composites by friction stir welding assisted by electrical current, Mater. Des. 113 (2017) 311–318.
[16] T. Peat, A. Galloway, A. Toumpis, R. Steel, W.Z. Zhu, N. Iqbal, Enhanced erosion performance of cold spray co-deposited AISI316 MMCs modified by friction stir processing, Mater. Des. 120 (2017) 22–35.
[17] K. Chu, X.H. Wang, Y.B. Li, D.J. Huang, Z.R. Geng, X.L. Zhao, H. Liu, H. Zhang, Thermal properties of graphene/metal composites with aligned graphene, Mater. Des. 140 (2018) 85–94.
[18] A.T. Miranda, L. Bolzoni, N. Barekar, Y. Huang, J. Shin, S.H. Ko, B.J. McKay, Processing, structure and thermal conductivity correlation in carbon fibre reinforced aluminium metal matrix composites, Mater. Des. 156 (2018) 329–339.
[19] J.W. Geng, G. Liu, F.F. Wang, T.R. Hong, J.C. Dai, M.L. Wang, D. Chen, N.H. Ma, H.W. Wang, Microstructural correlated damage mechanisms of the high-cycle fatigued in-situ TiB_2/Al-Cu-Mg composite, Mater. Des. 135 (2017) 423–438.
[20] Q.Q. Han, Y.Q. Geng, R. Setchi, F. Lacan, D.D. Gu, S.L. Evans, Macro and nanoscale wear behaviour of Al-Al_2O_3 nanocomposites fabricated by selective laser melting, Compos. Part B Eng. 127 (2017) 26–35.
[21] Z.Y. Ma, Y.L. Li, Y. Liang, F. Zheng, J. Bi, S.C. Tjong, Nanometric Si_3N_4 particulate-reinforced aluminum composite, Mater. Sci. Eng. A 219 (1996) 229–231.
[22] N. Samer, J. Andrieux, B. Gardiola, N. Karnatak, O. Martin, H. Kurita, L. Chaffron, S. Gourdet, S. Lay, O. Dezellus, Microstructure and mechanical properties of an Al-TiC metal matrix composite obtained by reactive synthesis, Compos. Part A Appl. S. 72 (2015) 50–57.
[23] J. Zhang, Q.B. Ouyang, Q. Guo, Z.Q. Li, G.L. Fan, Y.S. Su, L. Jiang, E.J. Lavernia, J.M. Schoenung, D. Zhang, 3D microstructure-based finite element modeling of deformation and fracture of SiCp/Al composites, Compos. Sci. Technol. 123 (2016) 1–9.
[24] A.A. Chernousov, Y.B. Chan, Optimising in-situ nitridation in piled aluminium flakes for novel closed cell composites with high fracture stress and toughness, Mater. Des. 150 (2018) 113–123.
[25] Q.Y. Hu, H.D. Zhao, F.D. Li, Microstructures and properties of SiC particles reinforced aluminum–matrix composites fabricated by vacuum–assisted high pressure die casting, Mater. Sci. Eng. A 680 (2017) 270–277.
[26] R.G. Munro, Material properties of titanium diboride, J. Res. Natl. Inst. Stand. Technol. 105 (2000) 709–720.
[27] X.X. Dong, X.Z. Zhu, S. Ji, Effect of super vacuum assisted high pressure die casting on the repeatability of mechanical properties of Al-Si-Mg-Mn die-cast alloys, J. Mater. Process. Technol. 266 (2019) 105–113.
[28] X.X. Dong, L.J. He, G.B. Mi, P.J. Li, Two directional microstructure and effects of nanoscale dispersed Si particles on microhardness and tensile properties of AlSi7Mg melt-spun alloy, J. Alloys Compd. 618 (2015) 609–614.
[29] X.P. Niu, B.H. Hu, I. Pinwill, H. Li, Vacuum assisted high pressure die casting of aluminium alloys, J. Mater. Process. Technol. 105 (2000) 119–127.
[30] X.Y. Shi, D.J. Li, A.A. Luo, B. Hu, L. Li, X.Q. Zeng, W.J. Ding, Microstructure and mechanical properties of Mg-7Al-2Sn alloy processed by super vacuum die-casting, Metall. Mater. Trans A 44 (2013) 4788–4799.
[31] Q.L. Wang, S.M. Xiong, Vacuum assisted high-pressure die casting of AZ91D magnesium alloy at different slow shot speeds, Trans. Nonferrous Metals Soc. China 24 (2014) 3051–3059.
[32] K.V. Yang, P. Rometsch, C.H.J. Davies, A.J. Huang, X.H. Wu, Effect of heat treatment on the microstructure and anisotropy in mechanical properties of A357 alloy produced by selective laser melting, Mater. Des. 154 (2018) 275–290.
[33] S. Lakshmi, L. Lu, M. Gupta, In situ preparation of TiB_2 reinforced Al based composites, J. Mater. Process. Technol. 73 (1998) 160–166.
[34] F. Long, X.H. Guo, K.X. Song, S.G. Jia, V. Yakubov, S.L. Li, S.H. Liang, Enhanced arc erosion resistance of TiB_2/Cu composites reinforced with the carbon nanotube network structure, Mater. Des. 183 (2019)(UNSP 108136).
[35] X.X. Dong, H. Youssef, Y.J. Zhang, S.H. Wang, S.X. Ji, High performance Al/TiB_2 composites fabricated by nanoparticle reinforcement and cutting-edge super vacuum assisted die casting process, Compos. Part B Eng. 177 (2019), 107453.
[36] Y. Tang, Z. Chen, A. Borbély, G. Ji, S.Y. Zhong, D. Schryvers, V. Ji, H.W. Wang, Quantitative study of particle size distribution in an in-situ grown Al–TiB_2 composite by synchrotron X-ray diffraction and electron microscopy, Mater. Charact. 102 (2015) 131–136.
[37] X.X. Dong, S.X. Ji, Si poisoning and promotion on the microstructure and mechanical properties of Al–Si–Mg cast alloys, J. Mater. Sci. 53 (2018) 7778–7792.

[38] X.X. Dong, Y.J. Zhang, S. Amirkhanlou, S.X. Ji, High performance gravity cast Al9Si0.45Mg0.4Cu alloy inoculated with AlB_2 and TiB_2, J. Mater. Process. Technol. 252 (2018) 604–611.
[39] X.X. Dong, L.J. He, P.J. Li, Gradient microstructure and multiple mechanical properties of AlSi9Cu alloy ribbon produced by melt spinning, J. Alloys Compd. 612 (2014) 20–25.
[40] S.J. Andersen, H.W. Zandbergen, J. Jansen, C. Traeholt, U. Tundal, O. Reiso, The crystal structure of the β″ phase in Al–Mg–Si alloys, Acta Mater. 46 (1998) 3283–3298.
[41] Z.P. Que, Y. Wang, Z. Fan, Formation of the Fe-containing intermetallic compounds during solidification of Al-5Mg-2Si-0.7Mn-1.1Fe alloy, Metall. Mater. Trans. A 49 (2018) 2173–2181.
[42] X.P. Li, G. Ji, Z. Chen, A. Addad, Y. Wu, H.W. Wang, J. Vleugels, J. Van Humbeeck, J.P. Kruth, Selective laser melting of nano-TiB_2 decorated AlSi10Mg alloy with high fracture strength and ductility, Acta Mater. 129 (2017) 183–193.
[43] X.X. Dong, Y.J. Zhang, S.X. Ji, Enhancement of mechanical properties in high silicon gravity cast AlSi9Mg alloy refined by Al3Ti3B master alloy, Mater. Sci. Eng. A 700 (2017) 291–300.
[44] X.X. Dong, H.L. Yang, X.Z. Zhu, S. Ji, High strength and ductility aluminium alloy processed by high pressure die casting, J. Alloys Compd. 773 (2019) 86–96.
[45] X.X. Dong, S. Amirkhanlou, S.X. Ji, Formation of strength platform in cast Al–Si–Mg–Cu alloys, Sci. Rep. 9 (2019) 9582.
[46] S. Bagherifard, N. Beretta, S. Monti, M. Riccio, M. Bandini, On the fatigue strength enhancement of additive manufactured AlSi10Mg parts by mechanical and thermal post-processing, Mater. Des. 145 (2018) 28–41.
[47] F. Sebek, J. Petruska, P. Kubik, Lode dependent plasticity coupled with nonlinear damage accumulation for ductile fracture of aluminium alloy, Mater. Des. 137 (2018) 90–107.